

Non-linear optics at twist interfaces in h-BN/SiC heterostructures

Abhijit Biswas,^{1,11,12} Rui Xu^{1,11}, Gustavo A. Alvarez^{2,11}, Jin Zhang^{3,11}, Joyce Christiansen-Salameh², Anand B. Puthirath¹, Kory Burns⁴, Jordan A. Hachtel⁵, Tao Li⁶, Sathvik Ajay Iyengar¹, Tia Gray¹, Chenxi Li¹, Xiang Zhang¹, Harikishan Kannan¹, Jacob Elkins¹, Tymofii S. Pieshkov^{1,7}, Robert Vajtai¹, A. Glen Birdwell⁸, Mahesh R. Neupane⁸, Elias J. Garratt⁸, Tony Ivanov⁸, Bradford B. Pate⁹, Yuji Zhao⁶, Hanyu Zhu^{1,12}, Zhiting Tian^{2,12}, Angel Rubio^{3,10,12} & Pulickel M. Ajayan^{1,12}

¹Department of Materials Science and Nanoengineering, Rice University, Houston, TX, 77005, USA

²Sibley School of Mechanical and Aerospace Engineering, Cornell University, Ithaca, NY 14853, USA

³Max Planck Institute for the Structure and Dynamics of Matter and Center for Free-Electron Laser Science, Luruper Chaussee 149, 22761 Germany

⁴Department of Materials Science & Engineering, University of Virginia, Charlottesville, VA 22904, USA

⁵Center for Nanophase Materials Sciences, Oak Ridge National Laboratory, Oak Ridge, TN 37831, USA

⁶Department of Electrical and Computer Engineering, Rice University, Houston, TX, 77005, USA

⁷Applied Physics Graduate Program, Smalley-Curl Institute, Rice University, Houston, TX, 77005, USA

⁸DEVCOM Army Research Laboratory, RF Devices and Circuits, Adelphi, Maryland 20783, USA

⁹Chemistry Division, Naval Research Laboratory, Washington, DC, 20375 USA

¹⁰Center for Computational Quantum Physics (CCQ), Flatiron Institute, New York 10010, New York, USA

¹¹These authors contributed equally to this work

¹²Corresponding Authors: **abhijit.biswas@rice.edu**, **hanyu.zhu@rice.edu**, **zhiting@cornell.edu**, **angel.rubio@mpsd.mpg.de**, **ajayan@rice.edu**

Abstract

Understanding the emergent electronic structure in twisted atomically thin layers has led to the exciting field of twistronics. However, practical applications of such systems are challenging since the specific angular correlations between the layers must be precisely controlled and the layers have to be single crystalline with uniform atomic ordering. Here, we suggest an alternative, simple and scalable approach where nanocrystalline two-dimensional (2D) film on three-dimensional (3D) substrates yield twisted-interface-dependent properties. Ultrawide-bandgap hexagonal boron nitride (h-BN) thin films are directly grown on high in-plane lattice mismatched wide-bandgap silicon carbide (4H-SiC) substrates to explore the twist-dependent structure-property correlations. Concurrently, nanocrystalline h-BN thin film shows strong non-linear second-harmonic generation and ultra-low cross-plane thermal conductivity at room temperature, which are attributed to the twisted domain edges between van der Waals stacked nanocrystals with random in-plane orientations. First-principles calculations based on time-dependent density functional theory manifest strong even-order optical nonlinearity in twisted h-BN layers. Our work unveils that directly deposited 2D nanocrystalline thin film on 3D substrates could provide easily accessible twist-interfaces, therefore enabling a simple and scalable approach to utilize the 2D-twistronics integrated in 3D material devices for next-generation nanotechnology.

Keywords: Twistronics, h-BN films, pulsed laser deposition, nano-domains, second harmonic generation, thermal conductivity, time dependent density functional theory

Twisting of two-dimensional van der Waals (2D-vdW) materials and their heterostructures have recently become an emerging topic in materials science and condensed matter physics (coined as twistrionics)^{1,2,3}. Twist angles between 2D-layers (via the formation of moiré patterns) alter electrical, optical and magnetic properties, manifesting a wide-range of multifunctional properties and twistrionic systems^{4,5,6}. Among numerous 2D materials, graphene and hexagonal boron nitride (h-BN) have been widely researched and their twisted h-BN/graphene/h-BN heterostructures (moiré superlattices) have been studied, demonstrating emergent phenomena^{7,8,9,10}. Recently, studies have revealed “ferroelectric-like domains” due to the stacking of two h-BN layers at small twisted angles ($\theta < 1^\circ$), attributed to the interfacial elastic deformations^{11,12,13}. Ex-situ mechanical stacking of thin individual monolayers of exfoliated single crystal materials has been used for twistrionics, which is non-trivial and a time-consuming process⁶. Although the transfer assembly enables successful stacking of 2D layers with desired twist angles, future application of twistrionics would demand an alternative in-situ and clean approach for the mass production of twisted 2D-materials. Therefore, thin film growth of such 2D-materials with the inherent generation of twist-interfaces by exploiting the interfacial lattice mismatch between the films and underlying substrate templates would possibly be a feasible alternative method. Though recent studies on twisted epitaxial graphene on SiC have shown some promise as a platform for the fundamental study, the control of the twist angle between the layers remains technically challenging and non-trivial^{14,15,16}.

Structurally, among various polymorphs of BN, the most stable h-BN lattice forms a 2D-layered structure with hexagonal stacking, with an ultrawide-bandgap (UWBG) of ~ 5.9 eV^{17,18}. It is a centrosymmetric non-polar system with lattice parameters of $a = b = 2.50$ Å, $c = 6.661$ Å. It has unique functional properties, e.g., lightweight, chemical inertness, possesses excellent optical properties, anisotropic thermal conductivity, and high dielectric constant, making it an applicable inert and thin dielectric barrier as well as a heat-spreading/thermal isolation material in devices¹⁹. On the other hand, 4H-SiC is also a promising electronic material with a wide-bandgap (WBG) of ~ 3.2 eV¹⁷. It also forms a hexagonal lattice with a stacking sequence of ABCB and lattice parameters of $a = b = 3.08$ Å and $c = 10.08$ Å²⁰. It has a unique combination of fascinating properties, e.g., high chemical stability, and high breakdown voltage, making it very useful for high-power field effect transistors, bipolar storage capacitors, and ultraviolet detectors^{21,22,23}. Therefore, it could be envisioned that the growth of 2D h-BN on 3D 4H-SiC substrate with high in-plane lattice mismatch would require long-range commensurability, and to minimize (or release) the interfacial energy it may form unique structures with the consequent observation of emergent properties.

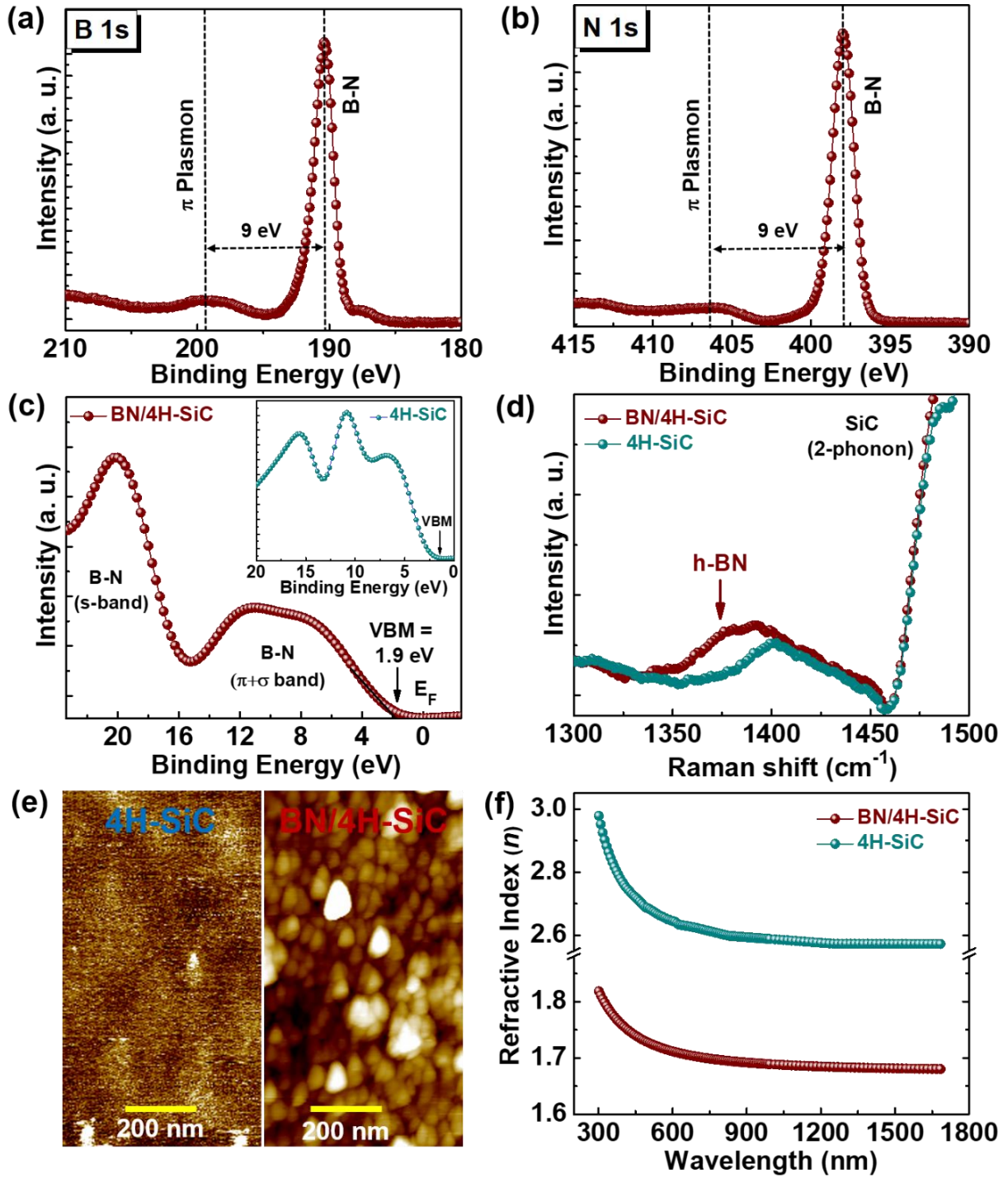


Fig. 1: Structural characterizations of h-BN films. (a), (b) B 1s core and N 1s core X-ray photoelectron spectroscopy shows the characteristics of B-N bonding along with the π -Plasmon peaks. (c) XPS valence-band spectrum (VBS) of the grown h-BN film. Inset shows the VBS of 4H-SiC substrate. (d) Raman spectra show a hump within ~ 1360 - 1380 cm^{-1} , corresponding to the transverse optical E_{2g} vibrations for in-plane B-N stretching in sp^2 bonded h-BN. (e) Atomic force microscopy surface morphology of 4H-SiC substrate and the BN film grown on it. (f) Refractive index of h-BN film and pristine 4H-SiC, in the visible to near infrared wavelength.

There have been several reports on h-BN thin film growth on pristine SiC or graphitized SiC substrates^{24,25,26,27,28,29,30}. Recently, reports contradict the crystalline nature of the grown h-BN film on graphene covered 6H-SiC. For example, Shin *et al.* grew epitaxial single-crystal h-BN/graphene lateral structure on Si-terminated 4H/6H-SiC (0001)²⁹. Very recently, Lin *et al.* have shown by performing comprehensive analysis that on 6H-SiC (0001), h-BN forms a hexagonal B_xN_y layer, rather than of high-quality stoichiometric epitaxial h-BN films³⁰.

Herein, we have grown 2D h-BN thin films grown on 4H-SiC substrates and demonstrated its twist-dependent structure-property correlations. In-depth spectroscopic and microscopic characterizations confirm the growth of nanocrystalline h-BN film. The film is found to be strongly second harmonic generation (SHG) active, also demonstrating modulation of photon counts with film thickness. Simultaneously, we obtained low cross-plane thermal conductivity, at room temperature. These coexisting properties are attributed to the twisted interfaces related to nano-domain edges in h-BN with random in-plane orientations, as supported by the first-principles time-dependent density functional theory calculations.

Growth and characterizations of h-BN films

We have grown h-BN thin films on commercially available *n*-type 4H-SiC (0001) substrates by using the pulsed laser deposition (PLD) (**Methods**). We performed the core level X-ray photoelectron spectroscopy (XPS) to characterize the BN films. B 1s core and N 1s core spectra show the presence of characteristic B-N bonding (~ 190.3 eV and ~ 398.1 eV), along with π -Plasmon peaks that correspond to h-BN (**Figs. 1a** and **1b** and Supplementary Information **Fig. S1**)^{31,32,33}. The atomic percentage of B:N was found to be $\sim 1:1$ (38.4:38.9 to be precise). The small hump around ~ 187.5 eV is due to the B-C peaks, possibly arising from an ambient air exposure related advantageous carbon effect. We also performed the XPS valence band spectroscopy (VBS) which shows the presence of two peaks, related to $\pi+\sigma$ band and *s*-band (**Fig. 1c**)^{34,35}. From VBS, we also found the valence band maxima (VBM) position at ~ 1.9 eV from the Fermi level (E_F). The characteristic VBS of 4H-SiC substrate is also shown (inset of **Fig. 1c**)³⁶. Furthermore, the Raman spectra show the presence of sp^2 bonded E_{2g} peak of h-BN around ~ 1370 - 1380 cm^{-1} , which corresponds to the in-plane E_{2g} vibrational mode of h-BN (**Fig. 1d**)³¹. The BN film E_{2g} peak intensity is significantly smaller than the surrounding two-phonon spectrum from the pristine 4H-SiC substrate. A similar trend in Raman spectra had also been observed in epitaxial graphene grown on SiC substrate^{37,38}, and it is attributed to the strong interfering signal arising from the SiC. The Raman spectra at various locations on the film are also shown (Supplementary Information **Fig. S2**).

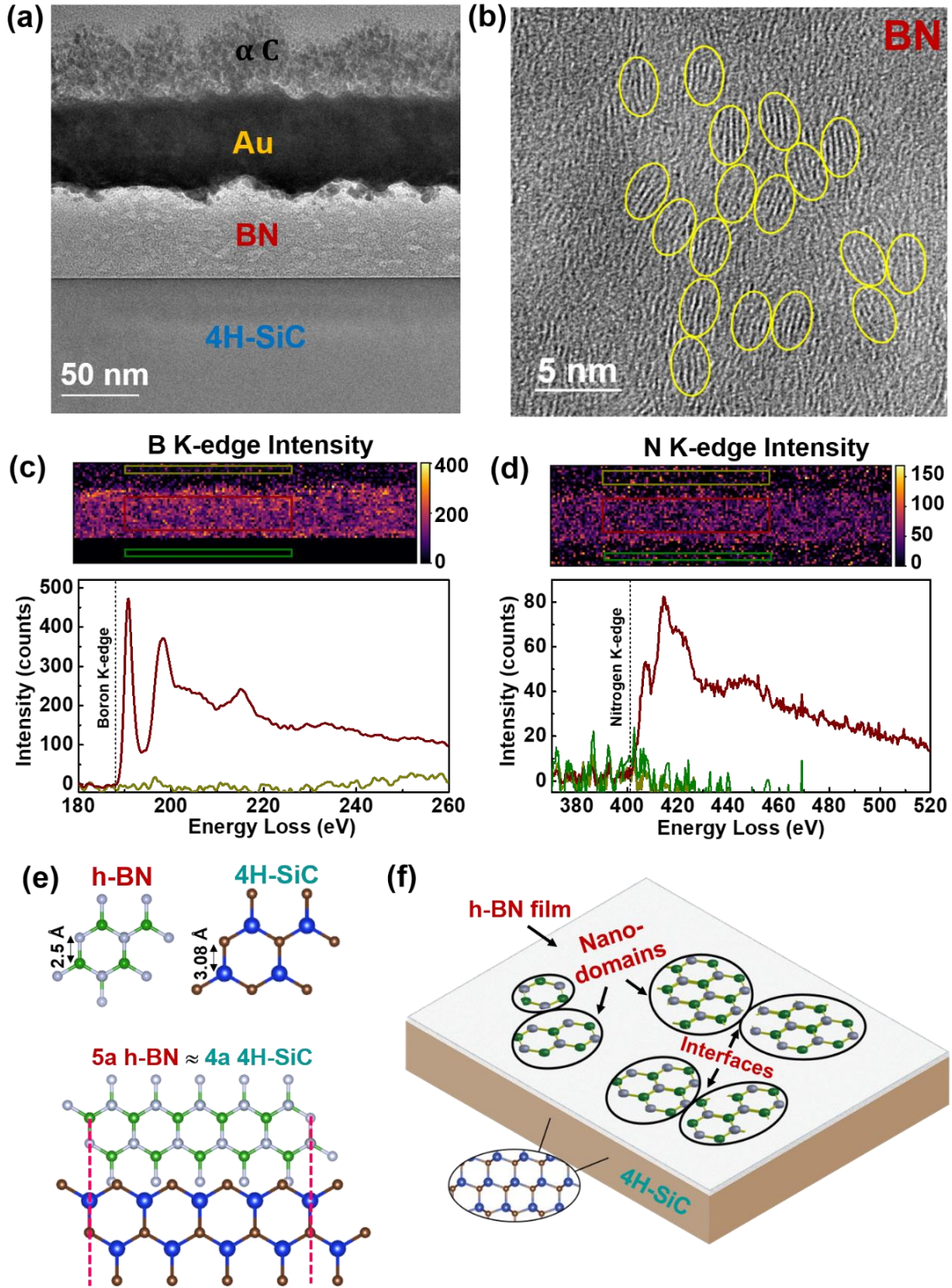


Fig. 2: Electron microscopy and crystal symmetry of h-BN/SiC. (a) High-resolution cross-sectional microscopic imaging of h-BN film on SiC. (b) Several nano-domains with crystalline fringes are visible (yellow regions). (c), (d) Core-loss electron-energy loss spectra (EELS) and B K-edge and N K-edge elemental mapping showing the uniform presence of B and N. (e) Top-view in-plane hexagonal structures of h-BN and 4H-SiC. Commensurate lattice matching between h-BN and 4H-SiC. (f) Nano-domains of h-BN and possible twisted interfaces.

The atomic force microscopy (AFM) image shows the triangular-shape-like morphology with lateral sizes of ~50-100 nm (**Fig. 1e**), compared with the smooth surface of bare single crystal 4H-SiC substrate. We also measured the refractive index (RI) of the film. In general, as shown in the literature, the RI value of crystalline h-BN flake is ~1.7-2.2, in the visible to near infrared (NIR) wavelength range, depending on the uncertainty of the thickness, roughness and crystallinity^{39,40}. In our case, we also observed a comparable RI value of ~1.7-1.8, in the similar wavelength range (whereas 4H-SiC single crystal substrate shows RI of ~2.6-2.9) (**Fig. 1f**). All these characterizations confirm the growth of h-BN films on 4H-SiC.

To get more information about crystalline quality of grown h-BN, we performed the cross-sectional high-resolution transmission electron microscopy (HRTEM) of h-BN/SiC film. For imaging, cross-sectional TEM lamella was prepared by a standard focused-ion-beam (FIB) method, based on mechanically thinning the sample followed by an Argon ion milling procedure. The cross-sectional bright-field image shows the interface between BN and SiC (**Fig. 2a**). While zoomed into the BN regions, interestingly, nano-domains with clear fringes are visible, embedded in uniform amorphous-like BN (**Fig. 2b**). The interplanar d -spacing of these fringes are ~0.33 nm, corresponds to the (0002) diffraction plane of h-BN (Supplementary Information **Fig. S3**)¹⁸. Moreover, the electron-energy loss spectra (EELS) in the BN region also confirms that it is h-BN, with a uniform distribution of B and N (**Figs. 2c and 2d**). Regarding the nanocrystalline growth, it is quite plausible, as the lattice mismatch between the h-BN film and 4H-SiC substrate is extremely high, with a tensile strain of ~23.2% (calculated as $\left(\frac{a_s - a_f}{a_f}\right) \times 100\%$ where a_s is the substrate and a_f is the film in-plane lattice constant) (**Fig. 2e**). Even the commensurate lattice matching (i.e. $5a_{\text{h-BN}} \approx 4a_{\text{4H-SiC}}$) would impose a strain of ~1.44% (**Fig. 2e**). Hence, to release such high interfacial energy, h-BN tends to form nanocrystalline ordering (**Fig. 2f**), instead of epitaxial film with long-range ordered structure, thereby forming random nano-domains with grain boundaries and twisted-interfaces.

Optical second harmonic generation and cross-plane thermal conductivity

The non-linear optical properties of vdW materials are sensitive to the stacking order.^{41,42} Broken inversion symmetry may lead to non-trivial topological electronic bands and more stable spin-orbit polarizations. In nanocrystalline h-BN, we expect various stacking faults resulting in local inversion symmetry breaking and cumulative finite SHG, which is prohibited in bulk single-crystalline h-BN. To test this hypothesis, we performed SHG imaging for h-BN films with various thicknesses grown on 4H-SiC. 4H-SiC belongs to space group P6₃mc and

forbids SHG for incident light along (0001) direction. Meanwhile, single crystalline monolayer h-BN is known to have finite SHG with a second-order nonlinear susceptibility ($\chi^{(2)}$) about ~ 20 pm/V for monolayer h-BN^{43,44,45}. For h-BN with an even number of layers, $\chi^{(2)}$ will vanish due to the restriction of structural symmetry⁴³. However, for nanocrystalline h-BN with sub-wavelength domain sizes, defects and random domain orientation may statistically result in finite SHG regardless of layer number^{44,46}.

Figure S4 illustrates the schematics of our scanning SHG microscopy (**Methods**). While bare 4H-SiC substrate has almost zero SHG signal, h-BN/SiC shows strong SHG signal from the sample area with high contrast against the background (**Fig. 3a** and Supplementary Information **Fig. S5**). The histogram of SHG photon count distribution for BN/SiC with different film thickness are shown (**Fig. 3b**). The effective $\chi^{(2)}$ of a 10 nm BN film is calculated to be ~ 3.3 pm/V, based on the experimental parameters and calibration with known samples (**Methods**). For 50 nm BN film, the effective $\chi^{(2)}$ is ~ 1.2 pm/V. This reduction of effective $\chi^{(2)}$ in thicker films is expected as SHG from randomly oriented domains scales linearly with the thickness (**Methods**). We also measured the SHG for h-BN films grown on sapphire and GaN substrates (Supplementary Information **Fig. S6**), on which films are either single-crystalline (on sapphire) or fully disordered (on GaN)^{46,47}. Comparatively, the SHG signal for nanocrystalline h-BN on 4H-SiC is found to be significantly higher (~ 25 times) than the film on these substrates (with an effective $\chi^{(2)}$ of ~ 0.10 pm/V)⁴⁶.

We measured the cross-plane thermal conductivity k_{\perp} of film using the optical pump-probe method of frequency-domain thermoreflectance (FDTR) (**Methods**). An electro-optic modulator (EOM) induced a sinusoidal intensity modulation on the pump, 488 nm continuous wave laser (from a signal generated by the lock-in amplifier), creating a periodic heat flux on the sample surface⁴⁸. An unmodulated, 532 nm continuous wave probe laser monitored the surface temperature through a change in surface reflectivity (Supplementary Information **Fig. S7**). Au was chosen as a transducer layer to maximize the coefficient of thermo-reflectance at the probe wavelength. We compared the measured phase lag of the probe beam (measured with respect to the reference signal from the lock-in amplifier) against the calculated phase lag of the sample surface temperature, induced by a periodic heat source at the sample surface⁴⁹. The sample is modeled as a three-layer system, where each layer includes the volumetric heat capacity c_p , cross-plane thermal conductivity k_{\perp} , in-plane thermal conductivity k_{\parallel} , layer thickness, and the thermal boundary conductance G_1 and G_2 (inset of **Fig. 3c**).

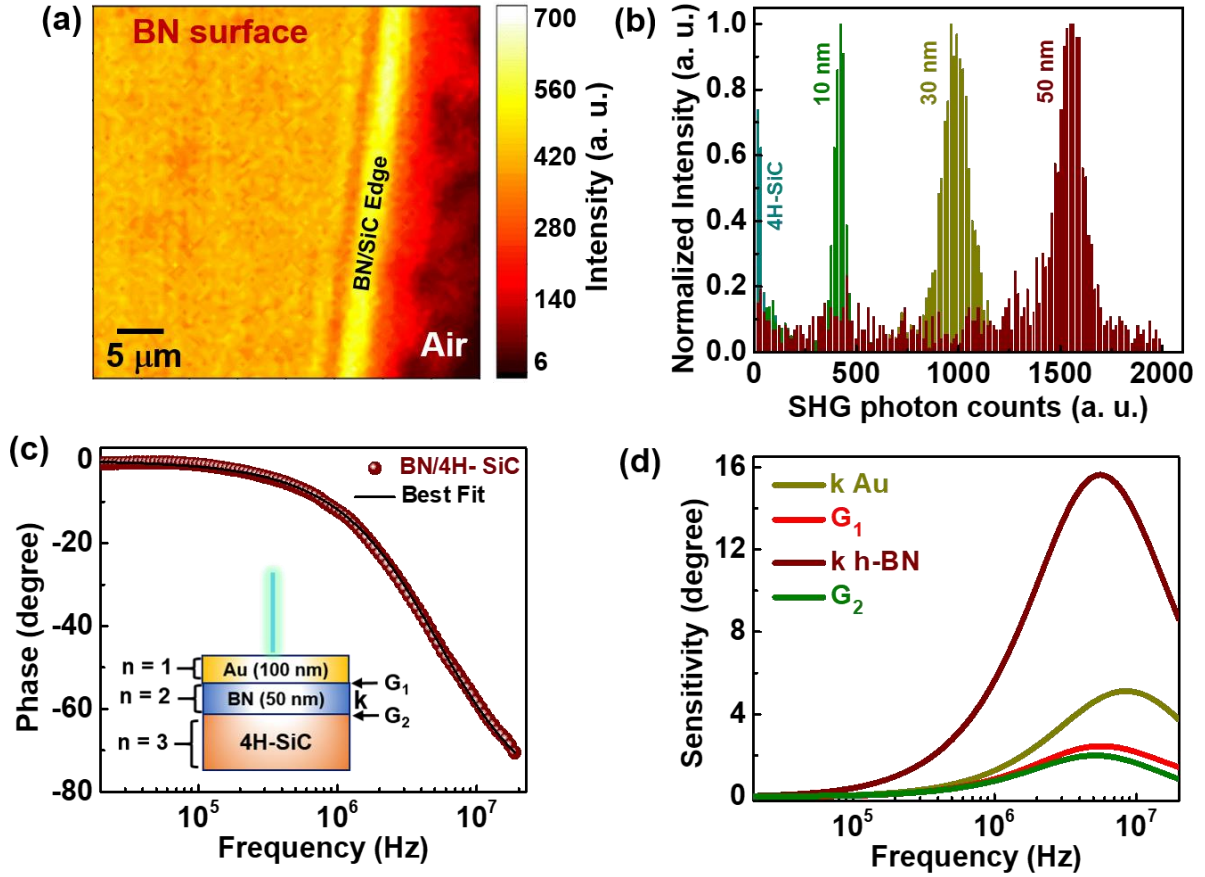


Fig. 3: Optical second harmonic generation and cross-plane thermal conductivity of h-BN.

(a) Spatial SHG intensity mapping of h-BN surface. (b) SHG photon count histogram of pristine 4H-SiC and h-BN/SiC with varying thickness. Large contrast can be observed from all three h-BN/SiC thin films compared with bare 4H-SiC. The histogram intensity is normalized by the highest count in each sample separately. (c) Phase vs. frequency data obtained from FDTR measurements shows a good approximation to the calculated best-fit curve. Inset shows the multilayer sample model. (d) Sensitivity analysis of the thermal conductivity of the Au transducer layer, the thermal boundary conductance G_1 , G_2 , and h-BN.

An example of the phase vs frequency data obtained from FDTR of an average of three runs acquired on one spot location (**Fig. 3c**). The data is in good approximation to the best-fit curve obtained from solving the heat diffusion equation. A more comprehensive description of solving this equation is detailed by Schmidt *et al*^{49,50}. We used the analytical method to estimate the uncertainty of our fitted data based on the parameters and measurement⁵⁰. Sensitivity analysis is used to help us determine which parameters can be fit together (Supplementary Information). The cross-plane thermal conductivity k_{\perp} , of h-BN is the parameter of interest and it is most sensitive at higher frequencies (**Fig. 3d**). The thermal boundary conductance G_1 between Au and the epitaxial h-BN, G_2 between h-BN and the bulk SiC substrate, and k of Au

are most sensitive at higher frequencies. Hence the focus was primarily on fitting the k of h-BN. At room temperature, the average k_{\perp} of three runs (measured at three different spot locations) of grown h-BN film was found to be $0.47 \pm 0.04 \text{ Wm}^{-1}\text{K}^{-1}$, which is one order lower than the bulk crystalline h-BN⁵¹.

Discussion on the structure-property correlations

Based on the strong SHG signal and lower cross-plane thermal conductivity, we introduce the recently proposed concept of “twist-optics” by Yao et al., originating from the twisted interfaces⁵². They found that by tuning the twist-angles between the h-BN layers, SHG intensity could even be modulated by a factor of ~ 50 (for our nanocrystalline h-BN film it is ~ 25 times). Since the artificial alternation of layers can break the local symmetry at buried vdW-interfaces, the second harmonics waves generated at each interface can be coherently harnessed which amplifies the nonlinear efficiency and the observation of a strong SHG signal.

On the other hand, nanocrystalline h-BN shows lower cross-plane thermal conductivity than its single crystalline counterpart⁵¹. As reported in the literature, bulk h-BN shows anisotropy in thermal conductivity with room temperature cross-plane thermal conductivity varying between $2\text{-}5 \text{ Wm}^{-1}\text{K}^{-1}$ ⁵¹. Recently, Jaffe *et al.*, investigated grain boundary effect in the lowering of thermal conductivity as they introduced the twisted sheets of BN with different thickness and random twist angles⁵³. They found the low cross-plane thermal conductivity of $\sim 0.26 \pm 0.01 \text{ Wm}^{-1}\text{K}^{-1}$ for a $\sim 74 \text{ nm}$ film by stacking the five twisted h-BN layers, which is ~ 7 times lower than the calculated thermal conductivity value of $\sim 2.0 \text{ Wm}^{-1}\text{K}^{-1}$. They attributed this lowering of cross-plane thermal conductivity to the twisted interfaces originating from the grain boundary effects. By using molecular-dynamics simulations it has been shown that twisted interfaces (i.e., grain boundaries) indeed act as strong phonon-phonon scattering centers, thus limiting the long phonon mean free paths at twist boundaries, and significantly reducing the cross-plane thermal conductivity⁵⁴.

The situation of “twist-interfaces” and thereby the twist-optics scenario can be envisioned here by illustrating a correlation between the h-BN films structure and properties. Here h-BN film layers are not deliberately (mechanically) twisted on SiC substrate; however, as can be seen from the HRTEM image, the h-BN film layers have random nano-ordered regions, which can be imagined as twist interfaces. As a result, symmetry is broken at these interfaces with the generation of collective second harmonic signals, resulting in strong SHG. Simultaneously, since these interfaces are randomly ordered, they induce strong phonon-phonon interactions, with the reduction of phonon mean free paths, thereby lowering the thermal conductivity.

Time-dependent density functional theory (TDDFT) for higher harmonics

For further insights about this twist-interface hypothesis, we performed extensive time-dependent density functional theory (TDDFT) calculations for higher harmonic generation (HHG) by twisting h-BN layers that have been demonstrated to exhibit a reliable description of the non-linear and non-perturbative responses of extended systems including h-BN heterostructures^{52,55,56,57}. Employing state-of-the-art simulations (see **Methods**), we analyzed high harmonic spectra for three twist angles ($\theta = 0^\circ$, 21.79° , and 60°) (**Fig. 4a**). To reduce the complexity and computational burden, we have not incorporated the complicated stacking orders, strain effect and structural relaxation effects, rather focused on the role of the twist angle on the calculated HHG spectra.

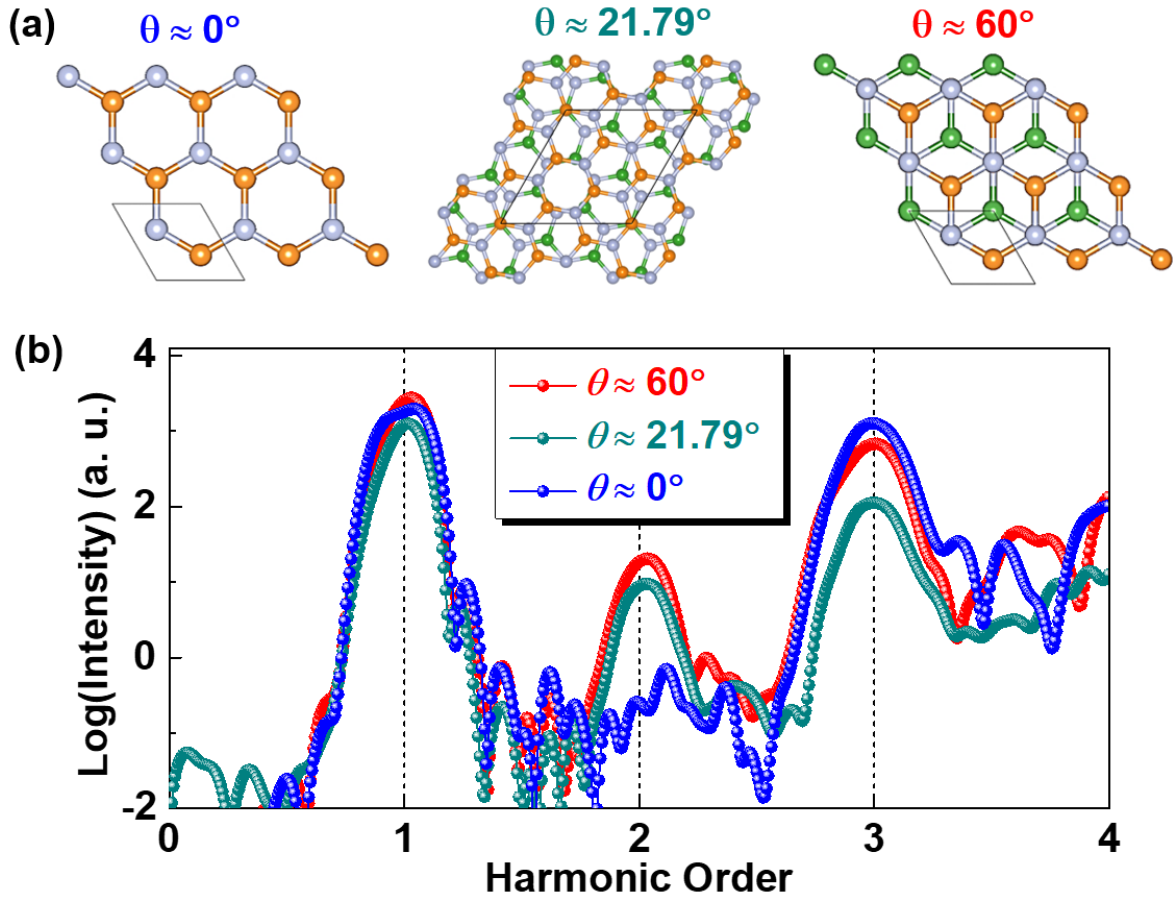


Fig. 4: Theoretical insights for the higher harmonic generation from twisted h-BN layers.

(a) Atomic structures of h-BN multilayers with different twist angles (θ). The white, orange and green spheres are nitrogen, boron (top layers) and boron (bottom layers), respectively (b) Higher harmonic spectra for h-BN layers with a twist angle of $\sim 0^\circ$, 21.79° and 60° , respectively, highlights the strength of second harmonics.

We find that the HHG spectrum of bulk h-BN changes significantly for the conditions with and without twists (**Fig. 4b**). The harmonic intensity is probed along with the corresponding applied laser pulse, which is parallel with the pump laser polarization. For the pristine AA' stacking ($\theta = 0^\circ$), clean odd harmonic peaks are observed for an excited pump laser (800 nm) while no clean even harmonics are obtained. However, for the $\theta = 21.79^\circ$ and 60° , HHG spectrum shows that the efficiency of second harmonics is significantly high. We observed ~ 27 and ~ 30 times increments in the second harmonic yield for the 21.79° and 60° twist cases, compared to the zero-twist angle (**Fig. 4b**). These results are in good agreement with previous theoretical predictions⁵⁸. The enhanced SHG is explained by the broken inversion symmetry from the phase difference in the adjacent layers in twisted h-BN layers, in contrast to the ideal non-twisted h-BN, which is an inversion-symmetric crystal in equilibrium⁵².

Conclusion

In summary, h-BN thin films grown on 4H-SiC substrates exhibit fascinating structural-property correlation. Film shows strong second harmonic generation signal and ultra-low cross-plane thermal conductivity, similar to the mechanically twisted single crystalline h-BN layers. Concurrent observations of strong second harmonics generation and low cross-plane thermal conductivity are attributed to the twisted-interfaces (randomly oriented nanocrystalline domains), harnessing the second-harmonic signal, as well as increasing the phonon-phonon scattering (low thermal conductivity). First-principles time-dependent density functional theory calculations for twisted h-BN layers supports the observation of strong even-order harmonic signals. Our work demonstrates that directly deposited thin films of 2D-vdW materials on 3D substrates could have significant twisted interface regions and application worthiness, enabling simple, scalable approaches to utilize 2D twistrionics integrated in 3D nanotechnology.

Methods

Thin film growth (Pulsed laser deposition, PLD):

We have grown various thicknesses of h-BN thin films on commercially available *n*-type (Nitrogen doped) 4H-SiC (0001) substrates (MSE Suppliers, USA) by using the load-lock assisted PLD (operating with a KrF laser of 248 nm wavelength and a 25ns pulse width) growth facility. Prior to the insertion, we cleaned the substrate in an ultrasonic bath with acetone. The base pressure of the main growth chamber was $\sim 5 \times 10^{-9}$ Torr, and the load-lock pressure was 5×10^{-8} Torr. We used a commercially available one-inch diameter h-BN target for the ablation. Films are grown at ~ 750 °C, and under 100 mTorr N₂ partial pressure. Prior to the growth, substrates are pre-annealed at the same growth temperature and pressure for ~ 15 min. Films are grown at 5 Hz repetition rate and with the laser energy of ~ 230 mJ (fluency ~ 2.2 J/cm²). The target-to-substrate distance was kept at ~ 50 mm. The laser spot size is ~ 1.5 mm \times 7 mm. Films are post-annealed for ~ 15 min at the same growth pressure and temperature to compensate for the nitrogen vacancies, and then cooled down to room temperature at ~ 20 °C/min. The average growth rate is found to be ~ 3.6 nm/min.

Structural, chemical, microscopic and optical characterizations (XPS, VBS, Raman, AFM, HRTEM and Refractive index):

X-ray photoelectron spectroscopy was performed by using PHI Quantera SXM scanning X-ray microprobe with 1486.6 eV monochromatic Al K α X-ray source. High-resolution XPS elemental scans and valence band spectra (VBS) were recorded at 26 eV and 69 eV pass energy. Park NX20 AFM was used to obtain surface topography, operating in tapping mode using Al-coated Multi75Al cantilevers. Raman spectroscopy was measured using a Renishaw inVia confocal microscope with a 532 nm laser used as the excitation source. For cross-sectional atomic scale imaging, the TEM specimens were prepared via a focused ion beam (FIB) milling process employing a Helios NanoLab 660 FIB unit (at Rice University) with gold to avoid discharging and amorphous carbon as protecting layers. The EELS spectra were acquired in Nion UltraSTEM unit (ORNL, USA) which was also equipped with a Gatan Enfina electron energy-loss (EEL) spectrometer to identify the elemental homogeneity of the sample with an EELS collection semi-angle of ~ 48 mrad. Variable angle spectroscopic ellipsometry (VASE) was applied to measure the refractive index (M-2000 Ellipsometer by J. A. Woollam Company) in the Class 100 (ISO 5) clean room facility at Rice University.

Optical second harmonic generation:

Second harmonic generation was performed using the home-built setup with a reflection geometry. A MaiTai (Spectra-Physics, USA) laser with 84 MHz repetition rate was used to give near-infrared pumping with the wavelength of 800nm and 40 fs pulse duration after optical compression. The laser is directed to a microscope with a scanning stage, which allows for spatially resolved SHG imaging, and then focused by a 20× objective to a spot size with a diameter of around 5.2 μm. The average laser power was kept at 10 mW at the sample location. The reflected signal is filtered by a 785 nm short-pass filter and a 400 nm bandpass filter to eliminate the reflected pump beam (Supplementary Information **Fig. S4**). The signal is finally detected using a single pixel photon counter (C11202-100, Hamamatsu, Japan). The calculation of effective $\chi^{(2)}$ is based on the method described elsewhere⁵⁹ for ultra-thin non-linear optical materials, followed by the equation:

$$P_{SHG} = \frac{16\sqrt{2}S|\chi_{eff}^{(2)}|^2\omega^2P_{in}^2}{c^3\varepsilon_0f\pi r^2t(1+n)^6} \quad (1)$$

Where $P_{SHG}(P_{in})$ is the averaged SHG signal (pump) power, χ_{eff}^2 is the effective χ^2 , $S=0.94$ is a shape factor for Gaussian pulses, ω is the frequency of pump light, c is the speed of light, ε_0 is the vacuum dielectric constant, f is the pump laser repetition rate, r is the radius of pump laser spot at focus, t is the pulse duration, and n is the refractive index of 4H-SiC substrate. We have also verified our calibration using monolayer CVD grown WS_2 samples with known $\chi^{(2)} \sim 0.7$ nm/V that after considering the collection efficiency for 400nm light ($\sim 10\%$), the output SHG power is about to be 4pW under the 1mW 800nm pumping pulse incidence. In polycrystalline materials, χ_{eff}^2 can be regarded as the sum effect of different domains, which is given by:

$$P_{SHG} \propto |\chi_{eff}^{(2)}|^2 = |\sum_n \chi_n^{(2)}|^2 \quad (2)$$

where χ_n^2 is the effective χ^2 of the n^{th} domain within the pump laser illumination volume on the sample. Since there is no correlation between each domain, Eq (2) can be rewritten as:

$$P_{SHG} \propto |\chi_{eff}^2|^2 = \sum_n |\chi_n^2|^2 \quad (3)$$

Assume the crystal quality is the same, P_{SHG} should be proportional to the number of domains within the pump laser illumination volume, which is linear proportional to sample thickness d , which is not what we observed in **Fig. 3b**. This indicates that for thicker samples the crystalline structures could be higher disordered.

Cross-plane thermal conductivity:

We measured the cross-plane thermal conductivity by using the optical pump-probe method of frequency-domain thermoreflectance (FDTR). An FDTR system is implemented with two continuous-wave lasers: a 488 nm pump and a 532 nm probe (Supplementary Information **Fig. S7**). The vertically polarized pump beam first travels through an optical isolator. The pump beam is focused into an electro-optic modulator (EOM), and a horizontally polarized beam is transmitted through a beam splitter (BS) and through a polarizing beam splitter (PBS). A microscope objective then focuses the beam onto the sample. The lock-in amplifier transmits a periodic signal to the EOM. The EOM then creates a periodic heat flux with a Gaussian spatial distribution on the sample surface. The probe beam first travels through an optical isolator and then through the BS, which coaxially aligns the probe beam with the pump beam. The probe beam, which is horizontally polarized, then travels through the PBS and passes through the quarter wave-plate, where the circularly polarized light is then focused by a microscope objective onto the sample (on the pump spot) to monitor the periodic fluctuations in reflectivity at the sample surface caused by the oscillating sample temperature. The post-sample is then reflected through the quarter-wave plate and reflected by the PBS to the photodetector.

First-principles calculation

The non-linear response functions of the heterostructure were obtained by evaluating the time-dependent electronic current computed by propagating the Kohn-Sham equations in real space and real time, as implemented in the Octopus code^{60,61,62}, with the adiabatic LDA functional⁶³. All calculations were performed using the fully relativistic Hartwigsen, Goedecker, and Hutter (HGH) pseudopotentials⁶⁴. In the simulations, we use three-layer h-BN on top and three-layer on the bottom to model the effect of interfaces. The laser pulses are treated classically in the dipole approximation (induced vector fields are imposed to be time-dependent but homogeneous in space) using the velocity gauge and we use a sin-square pulse envelope. The h-BN multilayers are sampled with six layers, including top three and bottom three layers, respectively. The real-space cell was sampled with a grid spacing of 0.4 Bohr and the Brillouin zone was sampled with a $42 \times 42 \times 21$ k-point grid to sample the Brillouin zone, which yielded highly converged results for h-BN. The BN bond length is taken here as the experimental value of 1.445 Å. We consider a laser pulse of 25-fs duration at full-width half-maximum (FWHM) with a sin-square envelope, and the carrier wavelength λ is 800 nm, corresponding to 1.55 eV. The HHG spectra are directly calculated from the time-dependent current $\mathbf{J}(\mathbf{r}, t)$ by a discrete

Fourier transform after a temporal derivative as

$$HHG(\omega) = \left| FT \left(\frac{\partial}{\partial t} \int d^3r J(r, t) \right) \right|^2 \quad (4)$$

Data availability

The data that support the findings of this study are available from the corresponding author upon reasonable request.

Acknowledgments

This work was sponsored partly by the Army Research Office and was accomplished under Cooperative Agreement Number W911NF-19-2-0269. The views and conclusions contained in this document are those of the authors and should not be interpreted as representing the official policies, either expressed or implied, of the Army Research Office or the U.S. Government. The U.S. Government is authorized to reproduce and distribute reprints for Government purposes notwithstanding any copyright notation herein. R. X. and H. Z. are supported by the are supported by Welch Foundation C-2128. T. Li and Y. Zhao is supported as part of ULTRA, an Energy Frontier Research Center funded by the US Department of Energy (DOE), Office of Science, Basic Energy Sciences (BES), under Award No. DE-SC0021230. This work is also supported by the Cluster of Excellence 'CUI: Advanced Imaging of Matter' of the Deutsche Forschungsgemeinschaft (DFG) - EXC 2056 - project ID 390715994, and SFB-925 "Light induced dynamics and control of correlated quantum systems" – project 170620586 of the Deutsche Forschungsgemeinschaft (DFG) and Grupos Consolidados (IT1453-22). We acknowledge support from the Max Planck-New York City Center for Non-Equilibrium Quantum Phenomena

Supporting Information

The online version contains supplementary material available at XXX.

Competing interests

The authors have no conflicts to disclose.

Author contributions

A. B., R. V., and P. M. A. conceptualized the study. A.B., C. L., T. G., X. Z., S. A. I., H. K., T. P., and J. E., grew and characterized the films. A. B. P., K. B., and J. H. performed the FIB and electron microscopy. T. L. and Y. Z. performed the refractive index measurement. R. X., and H. Z. carried out the second harmonic optical measurement. G. A., J. C., and Z. T. measured the thermal conductivity. J. Z., and A. R. performed the theoretical calculations and analysis. A. G. B., M. R. N., E. J. G., B. B. P., and T. I. commented on the manuscript. All the authors discussed the results and contributed on the manuscript preparation.

References

1. Andrei, E. Y. & MacDonald, A. H. **Graphene bilayers with a twist**, *Nat. Mater.* **19**, 1265 (2020).
2. Bistritzer, R. & MacDonald, A. H. **Moiré bands in twisted double-layer graphene**, *PNAS* **108**, 12233 (2011).
3. Wang, L. et al. **Correlated electronic phases in twisted bilayer transition metal dichalcogenides**, *Nat. Mater.* **19**, 861–866 (2020).
4. Dai, S., Xiang, Y. & Srolovitz, D. J. **Twisted Bilayer Graphene: Moiré with a Twist**, *Nano Lett.* **16**, 9, 5923–5927 (2016).
5. Cao, Y. et al. **Unconventional superconductivity in magic-angle graphene superlattices**, *Nature* **556**, 43 (2018).
6. Wu, D., Pan, Y. & Min, T. **Twistronics in Graphene, from Transfer Assembly to Epitaxy**, *Appl. Sci.* **10**, 4690 (2020).
7. Finney, N. R. et al. **Tunable crystal symmetry in graphene–boron nitride heterostructures with coexisting moiré superlattices**, *Nat. Nano.* **14**, 1029 (2019).
8. Yang, Y. et al. **In situ manipulation of van der Waals heterostructures for twistronics**, *Sci. Adv.* **6**: eabd3655 (2020).
9. Ribeiro-Palau, R., Zhang, C., Watanabe, K., Taniguchi, T., Hone, J. & Dean, C. R. **Twistable electronics with dynamically rotatable heterostructures**, *Science* **361**, 690–693 (2018).
10. Zheng, Z. et al. **Unconventional ferroelectricity in moiré heterostructures**, *Nature*, **588**, 71–76 (2020).
11. Woods, C. R. et al. **Charge-polarized interfacial superlattices in marginally twisted hexagonal boron nitride**, *Nat. Commun.* **12**, 347 (2021).
12. Yasuda, K., Wang, X., Watanabe, K., Taniguchi, T. & Jarillo-Herrero, P. **Stacking-engineered ferroelectricity in bilayer boron nitride**, *Science* **372**, 1458 (2021).
13. Bennett, D. & Ramez, B. **On electrically tunable stacking domains and ferroelectricity in moiré superlattices**, *npj 2D Mater. Appl.* **6**, 7 (2022).
14. Emtsev, K. V. et al. **Towards wafer-size graphene layers by atmospheric pressure graphitization of silicon carbide**, *Nat. Mater.* **8**, 203 (2009).
15. Cherkez, V., Laissardière, G., Mallet, P. & Veuillen, J. –Y. **Van Hove singularities in doped twisted graphene bilayers studied by scanning tunneling spectroscopy**, *Phys. Rev. B* **91**, 155428 (2015).

16. Hass, J. et al. **Why Multilayer Graphene on 4H-SiC(0001) Behaves Like a Single Sheet of Graphene**, *Phys. Rev. Lett.* **100**, 125504 (2008).
17. Tsao, J. Y. et al. **Ultrawide-Bandgap Semiconductors: Research Opportunities and Challenges**, *Adv. Electron. Mater.* **4**, 1600501 (2018).
18. Roy, S. et al. **Structure, Properties and Applications of Two-Dimensional Hexagonal Boron Nitride**, *Adv. Mater.* **33**, 2101589 (2021).
19. Bhimanapati, G. R., Glavin, N. R. & Robinson, J. A. **2D Boron Nitride: Synthesis and Applications**, *Semicond. Semimet.* **95**, 101 (2016).
20. Stockmeier, M., Müller, R., Sakwe, S. A., Wellmann, P. J. & Mager, A. **On the lattice parameters of silicon carbide**, *J. Appl. Phys.* **105**, 033511 (2009).
21. Liu, G., Tuttle, B. R. & Dhar, S. **Silicon carbide: A unique platform for metal-oxide-semiconductor physics**, *Appl. Phys. Rev.* **2**, 021307 (2015).
22. Langpoklakpam, C. et al. **Review of Silicon Carbide Processing for Power MOSFET**, *Crystals* **12**(2), 245 (2022).
23. Yi, A. et al. **Silicon carbide for integrated photonics**, *Appl. Phys. Rev.* **9**, 031302 (2022).
24. Sediri, H. et al. **Atomically Sharp Interface in an h-BN-epitaxial graphene van der Waals Heterostructure**, *Sci. Rep.* **5**, 16465 (2015).
25. Koch, R. J. et al. **Electronic structure of exfoliated and epitaxial hexagonal boron nitride**, *Phys. Rev. Mater.* **2**, 074006 (2018).
26. Guimon, C. et al. **XPS study of BN thin films deposited by CVD on SiC plane substrates**, *Surf. Interface Anal.* **16**, 440-445 (1990).
27. Kobayashi, Y. et al. **Boron Nitride Thin Films Grown on Graphitized 6H-SiC Substrates by Metalorganic Vapor Phase Epitaxy**, *Jpn. J Appl. Phys.* **46**, 2554–2557 (2007).
28. Majety, S. et al. **Hexagonal boron nitride and 6H-SiC heterostructures**, *Appl. Phys. Lett.* **102**, 213505 (2013).
29. Shin, H. et al. **Epitaxial Growth of a Single-Crystal Hybridized Boron Nitride and Graphene Layer on a Wide-Band Gap Semiconductor**, *J. Am. Chem. Soc.* **137**, 6897–6905 (2015).
30. Lin, Y. R. et al. **Boron nitride on SiC(0001)**, *Phys. Rev. Mater.* **6**, 064002 (2022).
31. Saha, S. et al. **Comprehensive characterization and analysis of hexagonal boron nitride on sapphire**, *AIP Advances* **11**, 055008 (2021).

32. Shen, T., Liu, S., Yan, W. & Wang, J. **Highly efficient preparation of hexagonal boron nitride by direct microwave heating for dye removal**, *J. Mater. Sci.* **54**, 8852 (2019).
33. Wang, G. et al. **Direct growth of hexagonal boron nitride films on dielectric sapphire substrates by pulsed laser deposition for optoelectronic applications**, *Fundam. res.* **1**, 677–683 (2021).
34. Widmayer, P. et al. **Electron spectroscopy on boron nitride thin films: Comparison of near-surface to bulk electronic properties**, *Phys. Rev. B* **59**, 5233 (1999).
35. Zhi, C. et al. **Weak morphology dependent valence band structure of boron nitride**, *J. Appl. Phys.* **114**, 054306 (2013).
36. Mahapatra, R. et al. **Energy-band alignment of gate dielectric stack**, *Appl. Phys. Lett.* **92**, 042904 (2008).
37. Röhrl, J. et al. **Raman spectra of epitaxial graphene on SiC(0001)**, *Appl. Phys. Lett.* **92**, 201918 (2008).
38. Lee, D. S. et al. **Raman Spectra of Epitaxial Graphene on SiC and of Epitaxial Graphene Transferred to SiO₂**, *Nano. Lett.* **8**, 4320-4325 (2008).
39. Rah, Y., Jin, Y., Kim, S. & Yu, K. **Optical analysis of the refractive index and birefringence of hexagonal boron nitride from the visible to near-infrared**, *Optics Lett.* **44**, 3797 (2019).
40. Franke, E. et al. **Phase and microstructure investigations of boron nitride thin films by spectroscopic ellipsometry in the visible and infrared spectral range**, *J. Appl. Phys.* **82**, 2906 (1997).
41. Deng, K. et al. **Experimental observation of topological Fermi arcs in type-II Weyl semimetal MoTe₂**, *Nat. Phys.* **12**, 1105–1110 (2016).
42. Zhao, M. et al. **Atomically phase-matched second-harmonic generation in a 2D crystal**, *Light: Science & Applications*, **5(8)**, e16131–e16131 (2016).
43. Li, Y. et al. **Probing Symmetry Properties of Few-Layer MoS₂ and h-BN by Optical Second-Harmonic Generation**, *Nano Lett.* **13**, 3329 (2013).
44. Kim, S. Et al. **Second-harmonic generation in multilayer hexagonal boron nitride flakes**, *Opt. Lett.* **44**, 5792 (2019).
45. Cunha, R. et al. **Second harmonic generation in defective hexagonal boron nitride**, *J. Phys.: Condens. Matter.* **32**, 19LT01 (2020).

46. Biswas, A. et al. **Properties and device performance of BN thin films grown on GaN by pulsed laser deposition**, *Appl. Phys. Lett.* **121**, 092105 (2022).
47. Biswas, A. et al. **Unidirectional domain growth of hexagonal boron nitride thin films**, *Appl. Mat. Today*, **30**, 101734 (2023).
48. Regner, K. T., Majumdar, S. & Malen, J. A. **Instrumentation of broadband frequency domain thermorefectance for measuring thermal conductivity accumulation functions**, *Rev. Sci. Instrum.* **84**, 064901 (2013).
49. Schmidt, A. J., Cheaito, R. & Chiesa, M. **A frequency-domain thermorefectance method for the characterization of thermal properties**, *Rev. Sci. Instrum.* **80**, 094901 (2009).
50. Yang, J., Ziade, E. & Schmidt, A. J. **Uncertainty analysis of thermorefectance measurements**, *Rev. Sci. Instrum.* **87**, 014901 (2016).
51. Jiang, P., Qian, X., Yang, R. & Lindsay, L. **Anisotropic thermal transport in bulk hexagonal boron nitride**, *Phys. Rev. Mater.* **2**, 064005 (2018).
52. Yao, K. et al. **Enhanced tunable second harmonic generation from twistable interfaces and vertical superlattices in boron nitride homostructures**, *Sci. Adv.* **7**, eabe8691 (2021).
53. Jaffe, G. R. et al. **Long Phonon Mean Free Paths Observed in Cross-plane Thermal-Conductivity Measurements of Exfoliated Hexagonal Boron Nitride**, arXiv:2103.07452v3.
54. Ouyang, W., Qin, H., Urbakh, M. & Hod, O. **Controllable Thermal Conductivity in Twisted Homogeneous Interfaces of Graphene and Hexagonal Boron Nitride**, *Nano Lett.* **20**, 10, 7513–7518 (2020).
55. Tancogne-Dejean, N. & Rubio, A. **Atomic-like high-harmonic generation from two-dimensional materials**, *Sci. Adv.* **4**, eaao520 (2018).
56. Neufeld, O., Zhang, J., De Giovannini, U. & Rubio, A. **Probing phonon dynamics with multidimensional high harmonic carrier-envelope-phase spectroscopy**, *PNAS* **119** (25), e2204219119 (2022).
57. Ginsberg, J. S. et al. **Optically-Induced Symmetry Breaking via Nonlinear Phononics**, arXiv:2107.11959.
58. Le Breton, G. et al. **High-harmonic generation from few-layer hexagonal boron nitride: Evolution from monolayer to bulk response**, *Phys. Rev. B* **98**, 165308 (2018).

59. Woodward, R. I. et al. **Characterization of the second- and third-order nonlinear optical susceptibilities of monolayer MoS₂ using multiphoton microscopy**, *2D Mater.* **4**, 011006 (2017).
60. Castro, A. et al. **Octopus: A Tool for the Application of Time-Dependent Density Functional Theory**, *Phys. Status Solidi* **243**, 2465 (2006).
61. Andrade, X. et al. **Real-space grids and the Octopus code as tools for the development of new simulation approaches for electronic systems**, *Phys. Chem. Chem. Phys.* **17**, 31371–31396 (2015).
62. Tancogne-Dejean, N. et al. **Octopus, a computational framework for exploring light-driven phenomena and quantum dynamics in extended and finite systems**, *J. Chem. Phys.* **152**, 124119 (2020).
63. G. Onida, L. Reining, & A. Rubio, **Electronic excitations: density-functional versus many-body Green's-function approaches**, *Rev. Mod. Phys.* **74**, 601–659 (2002).
64. Hartwigsen, C., Goedecker, S. & Hutter, J. **Relativistic separable dual-space Gaussian pseudopotentials from H to Rn**, *Phys. Rev. B* **58**, 3641–3662 (1998).
65. Schmidt, A. J., Chen, X. & Chen, G. **Pulse accumulation, radial heat conduction, and anisotropic thermal conductivity in pump-probe transient thermoreflectance**. *Rev. Sci. Instrum.* **79**, 114902 (2008).
66. Shen, W., Vaca, D. & Kumar, S. **Reconsidering Uncertainty from Frequency Domain Thermoreflectance Measurement and Novel Data Analysis by Deep Learning**, *Nanoscale Microscale Thermophys. Eng.* **24**, 1-12 (2020).

Supplementary information

Non-linear optics at twist interfaces in h-BN/SiC heterostructures

Abhijit Biswas,^{1,11,12} Rui Xu^{1,11}, Gustavo A. Alvarez^{2,11}, Jin Zhang^{3,11}, Joyce Christiansen-Salameh², Anand B. Puthirath¹, Kory Burns⁴, Jordan A. Hachtel⁵, Tao Li⁶, Sathvik Ajay Iyengar¹, Tia Gray¹, Chenxi Li¹, Xiang Zhang¹, Harikishan Kannan¹, Jacob Elkins¹, Tymofii S. Pieshkov^{1,7}, Robert Vajtai¹, A. Glen Birdwell⁸, Mahesh R. Neupane⁸, Elias J. Garratt⁸, Tony Ivanov⁸, Bradford B. Pate⁹, Yuji Zhao⁶, Hanyu Zhu^{1,12}, Zhiting Tian^{2,12}, Angel Rubio^{3,10,12} & Pulickel M. Ajayan^{1,12}

¹Department of Materials Science and Nanoengineering, Rice University, Houston, TX, 77005, USA

²Sibley School of Mechanical and Aerospace Engineering, Cornell University, Ithaca, NY 14853, USA

³Max Planck Institute for the Structure and Dynamics of Matter and Center for Free-Electron Laser Science, Luruper Chaussee 149, 22761 Germany

⁴Department of Materials Science & Engineering, University of Virginia, Charlottesville, VA 22904, USA

⁵Center for Nanophase Materials Sciences, Oak Ridge National Laboratory, Oak Ridge, TN 37831, USA

⁶Department of Electrical and Computer Engineering, Rice University, Houston, TX, 77005, USA

⁷Applied Physics Graduate Program, Smalley-Curl Institute, Rice University, Houston, TX, 77005, USA

⁸DEVCOM Army Research Laboratory, RF Devices and Circuits, Adelphi, Maryland 20783, USA

⁹Chemistry Division, Naval Research Laboratory, Washington, DC, 20375 USA

¹⁰Center for Computational Quantum Physics (CCQ), Flatiron Institute, New York 10010, New York, USA

¹¹These authors contributed equally to this work

¹²Corresponding Authors: abhijit.biswas@rice.edu, hanyu.zhu@rice.edu, zhiting@cornell.edu, angel.rubio@mpsd.mpg.de, ajayan@rice.edu

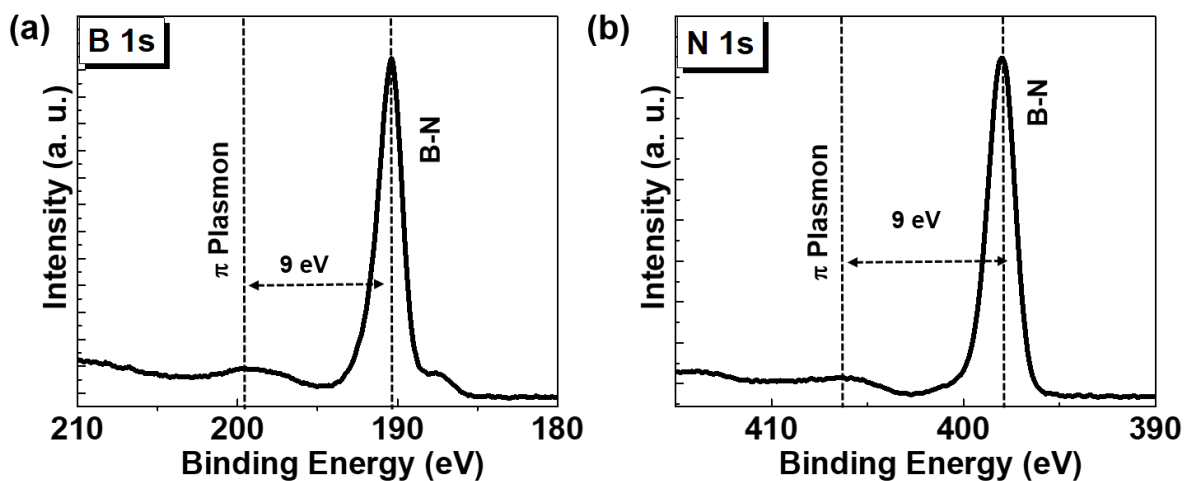


Fig. S1: Structural characterizations of a 10 nm h-BN film. (a), (b) B 1s core and N 1s core X-ray photoelectron spectroscopy shows the characteristics of B-N peaks.

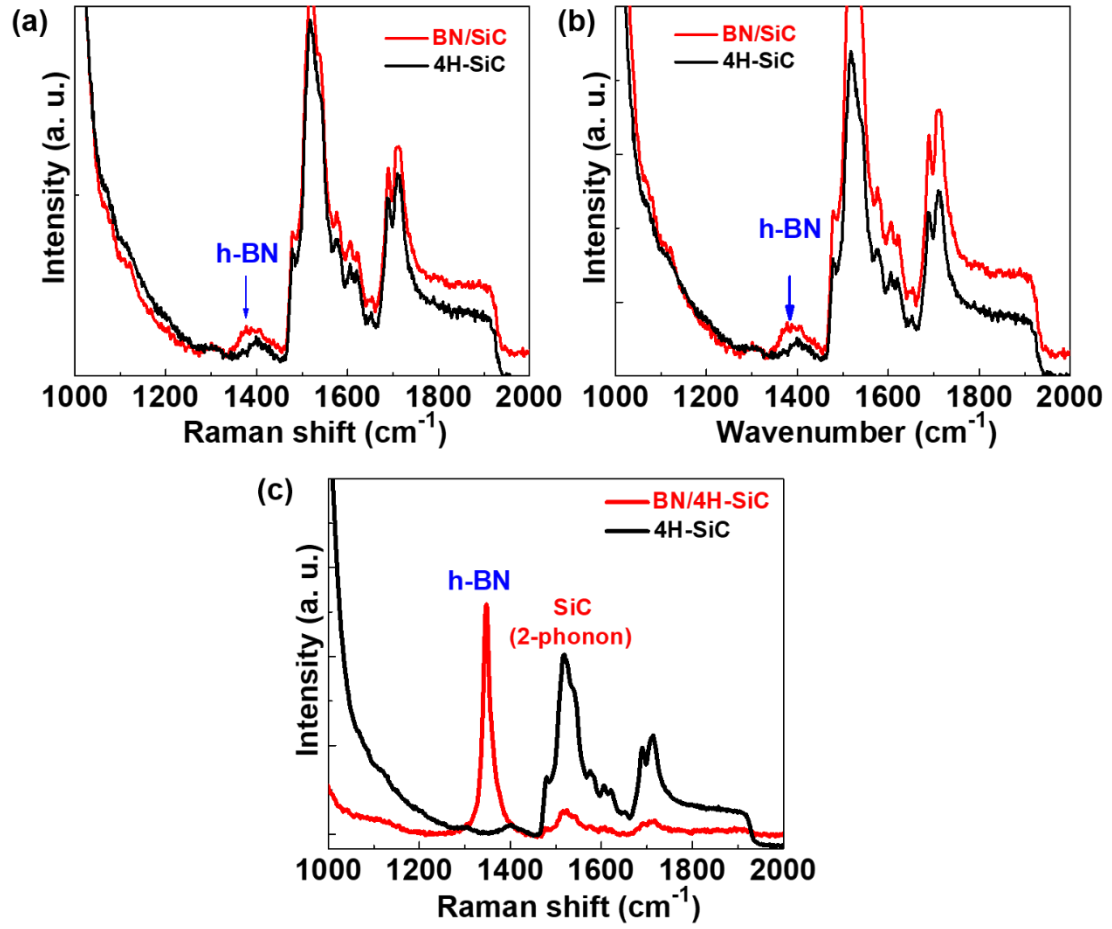


Fig. S2: (a), (b) Raman spectra at several places of a thin h-BN film showing a hump around $\sim 1360\text{-}1380\text{ cm}^{-1}$, corresponding to the transverse optical E_{2g} vibrations for in-plane B-N bond stretching in sp^2 bonded h-BN. (c) Raman spectra of a thick 300 nm BN/SiC film shows a clear E_{2g} h-BN peak.

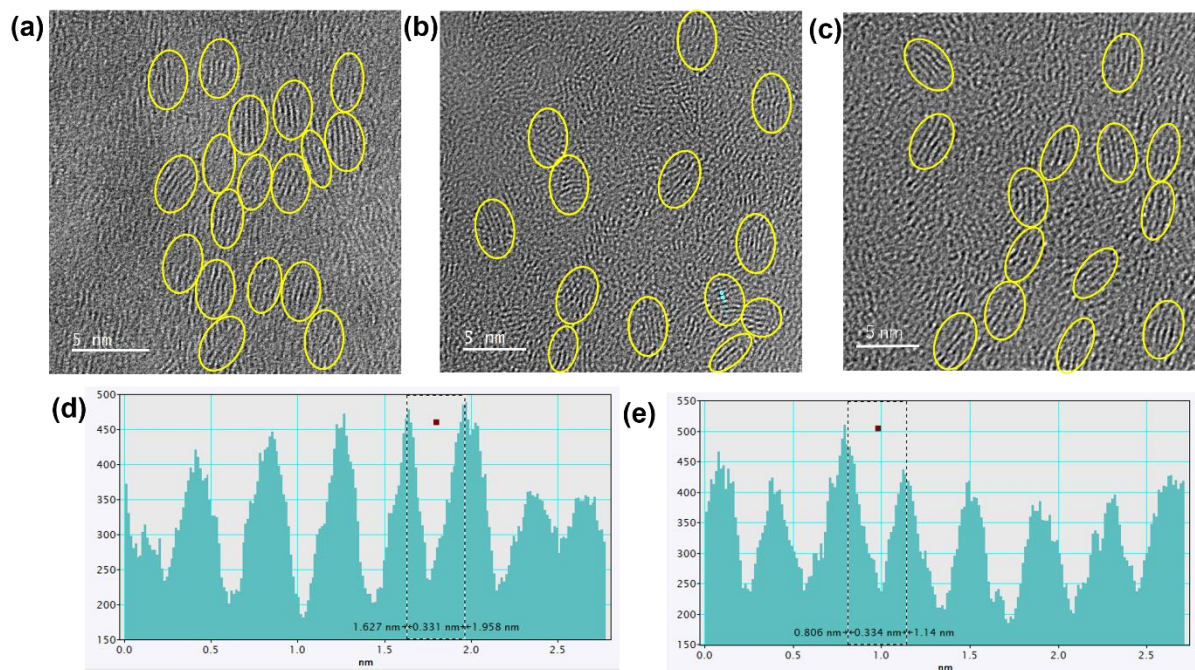


Fig. S3: (a)-(e) Several nano-domains with clear crystalline fringes (d -spacing of ~ 0.33 nm) are also observed, corresponding to interplanar d -spacing of (0002) h-BN.

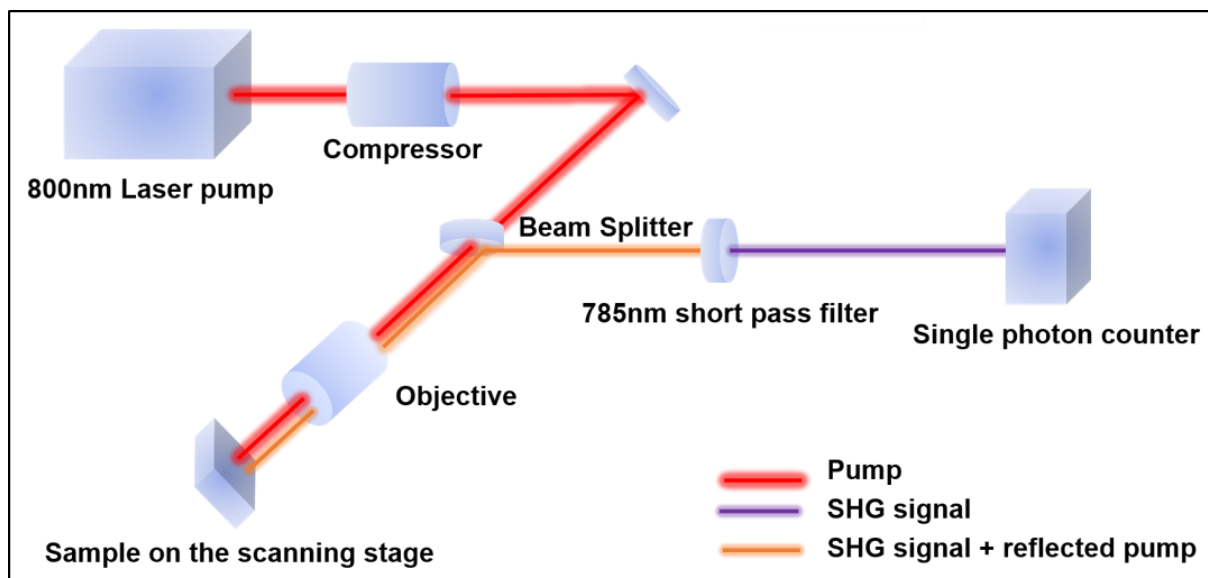


Fig. S4: Schematic of the second harmonic generation (SHG) excitation and collection from the h-BN film surface.

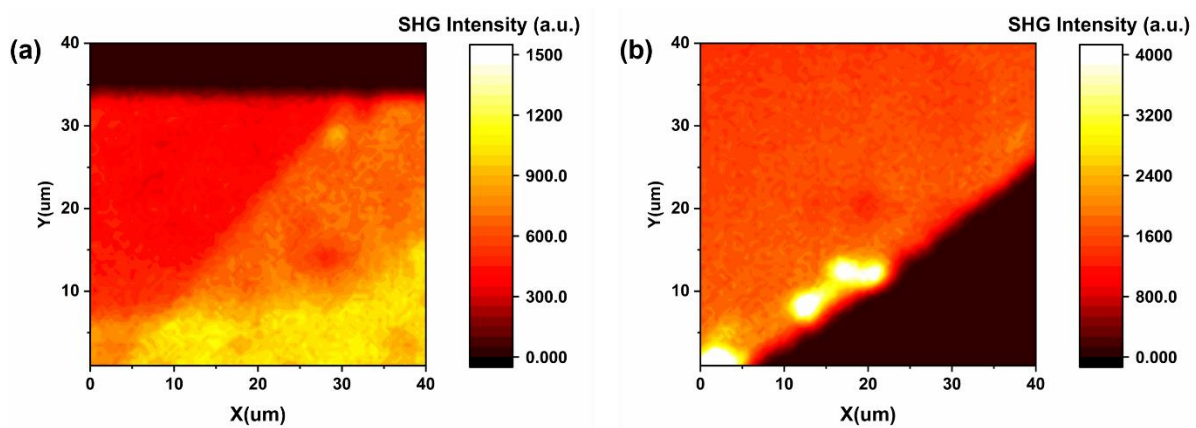


Fig. S5: (a), (b) Spatial SHG intensity mapping of 30 nm (left) and 50 nm (right) h-BN films.

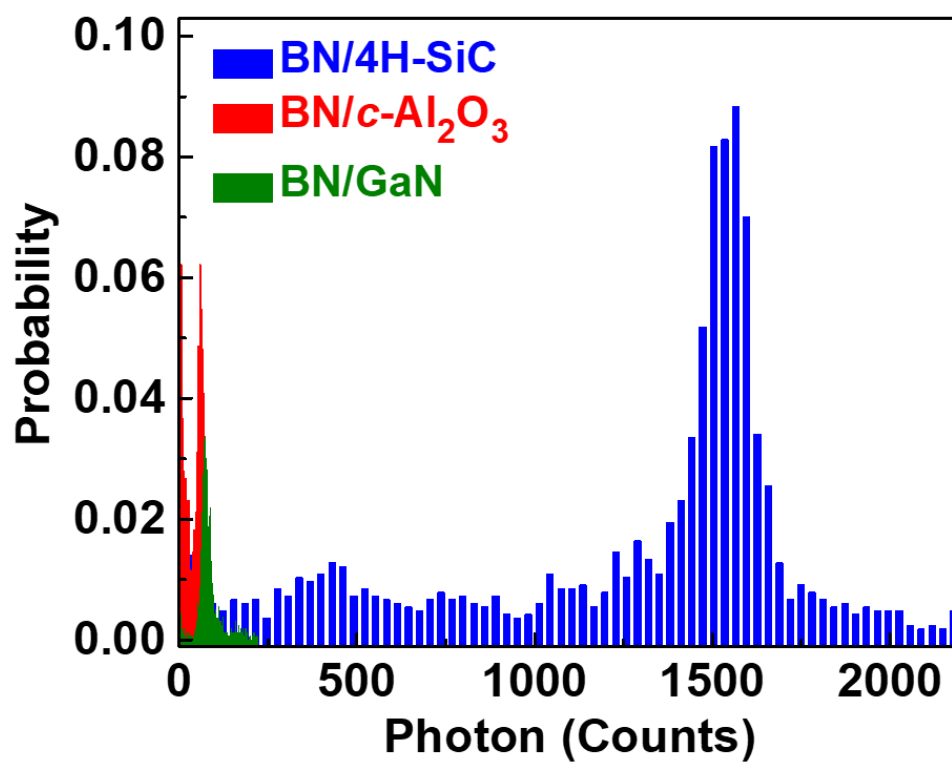


Fig. S6: Comparative SHG response of h-BN thin films grown on SiC, *c*-Al₂O₃ and GaN substrates, by using the same growth conditions, showing much larger SHG signal on SiC.

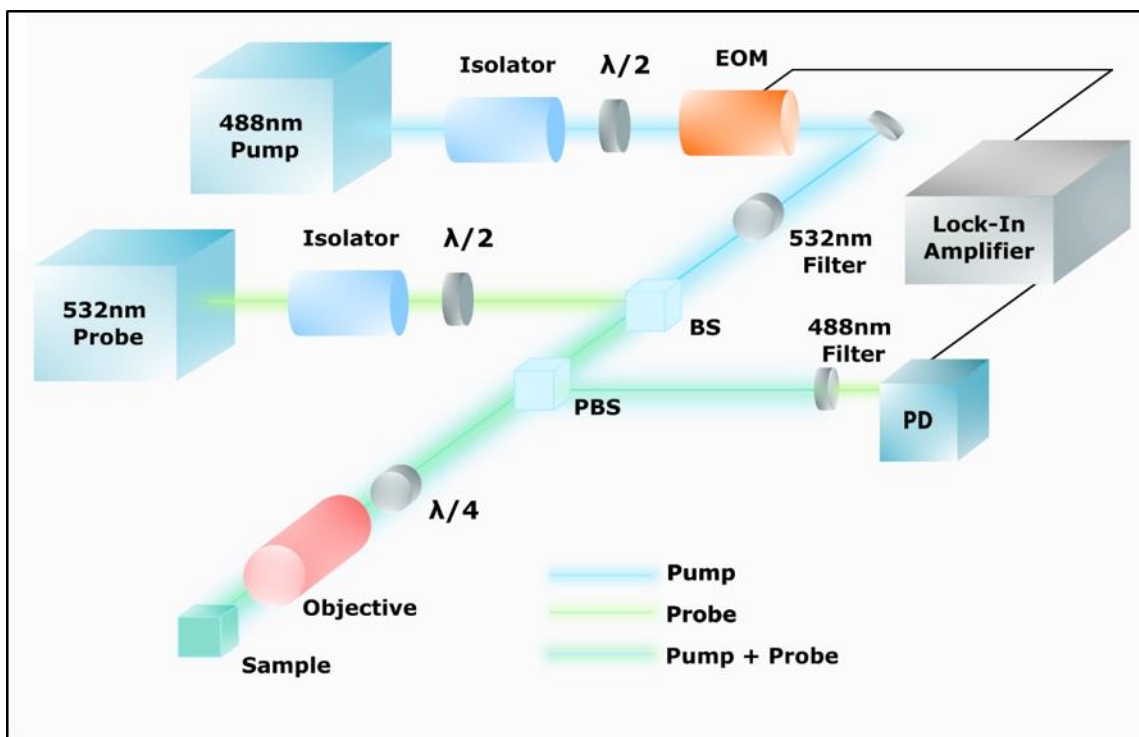


Fig. S7: Schematic of the FDTR setup for the thermal conductivity measurement.

Frequency-domain thermoreflectance (FDTR) details:

The detailed derivation of the mathematical model can be found elsewhere^{49,65}. The phase lag of the probe beam, measured with respect to the reference signal from the lock-in amplifier, is compared against the calculated phase lag of the sample surface temperature to a periodic Gaussian heat source at the sample surface⁴⁹. Mathematically, the solution to the calculated phase lag (based on individual materials physical properties of interest, in our case k and G_2) can be expressed as a complex number $Z(\omega_o)$, such that the output of the lock-in amplifier for a reference wave $e^{i\omega_o t}$ is given by

$$Ae^{i(\omega_o t + \phi)} = Z(\omega_o)e^{i\omega_o t} \quad (S1)$$

where ω_o is the modulation frequency, A is the amplitude, and ϕ the phase of the fundamental component of the probe signal with respect to the reference wave⁴⁹.

In the case of continuous-wave pump and probe beams

$$Z(\omega_o) = \beta H(\omega_o) \quad (S2)$$

where β is a factor including the thermoreflectance coefficient of the sample and the power of the pump and probe beams⁴⁹. $H(\omega_o)$ is the thermal frequency response of the sample weighted by the intensity of the probe beam⁴⁹. The weighted sample frequency response, $H(\omega_o)$, is obtained by solving the heat diffusion equation for a Gaussian heat source (the pump beam) impinging on a multilayer stack of materials and weighting the resulting temperature distribution at the top surface by the Gaussian intensity distribution of the probe beam⁴⁹.

As an example, for a single slab of material in the frequency domain, the temperature θ_t and the heat flux f_t on the top side of the slab are related to the temperature θ_b and the heat flux f_b on the bottom side through

$$\begin{bmatrix} \theta_b \\ f_b \end{bmatrix} = \begin{bmatrix} \cosh(qd) & \frac{-1}{k_{\perp}q} \sinh(qd) \\ -k_{\perp}q \sinh(qd) & \cosh(qd) \end{bmatrix} \begin{bmatrix} \theta_t \\ f_t \end{bmatrix} \quad (S3)$$

where d is the layer thickness, k_{\perp} the cross-plane thermal conductivity and

$$q^2 = \frac{k_{\parallel} \mathcal{H}^2 + \rho c i \omega}{k_{\perp}} \quad (\text{S4})$$

where \mathcal{H} is the Hankel transfer variable, ρ is the density, c is the specific heat capacity, and k_{\parallel} is the radial thermal conductivity.² The heat flux boundary condition at the top layer f_t is given by the Hankel transform of a Gaussian spot with power A_0 and $1/e^2$ radius of the pump beam on the surface w_0

$$f_t = \frac{A_0}{2\pi} \exp\left(\frac{-\mathcal{H}^2 w_0^2}{8}\right) \quad (\text{S5})$$

Multiple layers are handled by multiplying the matrices for individual layers together

$$\begin{bmatrix} \theta_b \\ f_b \end{bmatrix} = \mathbf{M}_n \mathbf{M}_{n-1} \dots \mathbf{M}_1 = \begin{bmatrix} A & B \\ C & D \end{bmatrix} \begin{bmatrix} \theta_t \\ f_t \end{bmatrix} \quad (\text{S6})$$

where \mathbf{M}_n is the matrix for the bottom layer⁴⁹. An interface conductance G is treated by taking the limit as the heat capacity of a layer approaches zero and choosing k_{\perp} and d such that $G = k_{\perp}/d$. Since we treat the n th layer as semi-infinite, Eq. (S5) reduces to

$$\theta_t = \frac{-D}{C} f_t \quad (\text{S7})$$

The final frequency $H(\omega)$ in real space is found by taking the inverse Hankel of Eq. (S6) and weighting the results by the probe intensity distribution, which is taken as a Gaussian spot with $1/e^2$ radius of the probe beam on the surface w_1

$$H(\omega_0) = \frac{A_0}{2\pi} \int_0^{\infty} \mathcal{H}\left(\frac{-D}{C}\right) \exp\left[\frac{-\mathcal{H}^2(w_0^2 + w_1^2)}{8}\right] d\mathcal{H} \quad (\text{S8})$$

This result is inserted into Eq. (S2), where the measurement of individual materials physical properties is performed as an inverse problem, minimizing the error between the lock-in phase data and the phase of Eq. (S2) via a non-linear least-squares algorithm⁴⁹.

Uncertainty Analysis:

We used the analytical method to estimate the uncertainty of our fitted data based on the parameters and measurement⁵⁰. We assumed uncertainty of 3% for the volumetric heat capacity⁵⁰, and 4% for the thicknesses of the Au transducer layer and AlN epilayer. To explore uncertainties of multiple unknown parameters, Jacobian matrices were used in the calculation. We selected the analytical method because it accumulates uncertainties from the parameters and measurements in the Jacobian matrices. The consideration of correlation would not overestimate the uncertainty⁶⁶. Given the measured signal Φ and known parameter matrix X_C , the variance-covariance matrix of unknown matrix X_U is

$$\text{var}(X_U) = (J'_U J_U)^{-1} J'_U (\text{var}(\Phi) + J_C \text{var}(X_C) J_C^{-1}) J_U (J'_U J_U)^{-1} \quad (\text{S9})$$

Here, $\text{var}(\Phi)$ and $\text{var}(X_C)$ are the diagonal matrices whose elements are variances of measured signal and known parameters, respectively⁴⁸. J_C and J_U are the Jacobian matrices of known and unknown parameters accordingly with the form:

$$J = \begin{pmatrix} \frac{\partial f(\omega_1, X)}{\partial x_1} | X^* & \dots & \frac{\partial f(\omega_1, X)}{\partial x_N} | X^* \\ \vdots & \ddots & \vdots \\ \frac{\partial f(\omega_M, X)}{\partial x_1} | X^* & \dots & \frac{\partial f(\omega_M, X)}{\partial x_N} | X^* \end{pmatrix} \quad (\text{S10})$$

where $f(\omega_M, X)$ is the function to calculate the phase lag between pump and probe signals, ω_i , $i = 1, \dots, M$ are the frequency that takes the measurement, x_j , $j = 1, \dots, N$ are the parameters and X^* is the matrix of the fitted data⁵⁰. The diagonal elements of $\text{var}(X_U)$ are the variances of the unknown parameters. Thus, this analysis consists of the propagation of errors and the variance among different measurement spots (i.e., the standard error of the six different spot locations, which is incorporated in $\text{var}(\Phi)$).